RESEARCH ARTICLE

International Journal of Climatology — RMetS

Long time series spatialized data for urban climatological studies: A case study of Paris, France

Benjamin Le Roy[1] 🟢 | **Aude Lemonsu**[1] | **Raphaëlle Kounkou-Arnaud**[2] | **Denis Brion**[2] | **Valéry Masson**[1]

[1]CNRM, Université de Toulouse, Météo-France, CNRS, Toulouse, France

[2]Direction Inter-régionale Île-de-France/Centre, Météo-France, Saint-Mandé, France

Correspondence
Benjamin Le Roy, Météo-France/CNRS, Centre National de Recherches Météorologiques, 42 avenue Gaspard Coriolis, 31057 Toulouse CEDEX, France.
Email: benjamin.leroy@meteo.fr

Abstract

Historically, the urban climate and its interaction with regional environment and larger-scale meteorological phenomena have been studied by comparing weather stations in urban and surrounding rural areas. Nevertheless, spatialized meteorological data are now available with different spatial resolutions, temporal frequencies, and time depths. Here with the Paris area as a case study, three products were selected for their comparable spatial resolution of 1 km, their daily frequency, and a minimum 15-year time period with substantial common overlap: the MODIS products for land surface temperature (2000–2016), daily maps of minimum and maximum 2-m air temperatures (2000–2017) based on a statistical method of spatialization, and the COMEPHORE analysis for precipitation (1997–2012). Several spatialized indicators were used to monitor the urban climate and its impact on local climate. The intensity and spatial extent of both the surface urban heat island (SUHI) and the urban heat island of urban canopy layer (UHI), as well as the effect of the city on precipitation, were characterized. Based on these indicators, a climatological study was made for the Paris urban area and its surroundings. The comparison of (S)UHI climatologies showed that both phenomena (qualified by their intensity and spatial extent) have comparable seasonalities and orders of magnitude at night. The maximum intensity is reached in July, with more than 60% of the city affected by high temperatures. However, the phenomena differ during the day: the SUHI is mostly driven by the differences in surface properties between urban and rural environments, whereas the UHI is more influenced by general wind circulation and local atmospheric turbulence. Finally, the COMEPHORE analysis highlighted the influence of the Paris urban area on rainfall. It is observed throughout the year with an excess in daily precipitation of 29% downwind of the city, with some seasonal variability showing a more pronounced effect in summer.

KEYWORDS

COMEPHORE precipitation analysis, MODIS land surface temperature, spatialized data, urban climate indicators, Urban Heat Island

1 | INTRODUCTION

Cities represent between 0.5 and 3% of the world surfaces (Liu *et al.*, 2014; Zhou *et al.*, 2015, 2018) but concentrate more than half of the population and are expected to grow by 2.5–3 billion inhabitants by the mid-century (UN, 2015).

Because of their physical properties, cities have an important effect on the atmosphere (Oke, 1973, 1995; Kalnay and Cai, 2003) and the local climate extending beyond their boundaries (Huff and Vogel, 1978; Shepherd, 2005; Oke *et al.*, 2017), which is now well documented (Arnfield, 2003; Grimmond, 2006; Souch and Grimmond, 2006; Oke *et al.*, 2017). The most studied phenomena are: the temperature difference between urban and rural areas known as the Urban Heat Island (UHI, Oke, 1973, 1995), the modifications of the energy balance (Oke, 1982, 1988), the changes in wind circulation and the structure of the surface boundary layer (Oke, 1995), and the alteration of precipitation rates (Shepherd, 2005).

Historically, urban climate studies were first made by comparing data from weather stations in the urban environment to those in surrounding rural areas (Lowry, 1974, 1977; Mills, 2014). Today, thanks to the progress made on measurement tools, on data processing and analysis, and on the understanding of the physical processes (Grimmond, 2006), an increasing number of studies is heading towards spatialized data (Tomlinson *et al.*, 2011; Zhou *et al.*, 2019). These datasets enable:

(1) A better monitoring and characterization of the urban signal and the real extent of its impact on the local climate.

(2) A better understanding of local physical processes resulting from the modification of the surfaces, and their interaction with larger scale phenomena (Roth *et al.*, 1989; Weng, 2009).

(3) The creation of databases on time series now reaching climatological scale, that is, a period long enough to represent the average climate without the daily variability.

(4) The definition of methodologies and indicators used for the study of extreme weather impacts on one hand, or the assessment of urbanization effects on the other hand (Schwarz *et al.*, 2012; Ward *et al.*, 2016).

(5) The evaluation of model performances (Hu *et al.*, 2014) and the assimilation of observational data in numerical weather prediction models.

The objective of this study is to build a spatialized and consistent database for the Paris urban area and its region by mapping an ensemble of meteorological variables (i.e., surface temperature, near-surface air temperature and precipitation rates). Thanks to a suitable spatial resolution, a daily temporal frequency, and a sufficiently long temporal depth, these data should allow a climatological monitoring of different aspects of the urban climate in Paris and of its interaction with the regional climate and larger scale meteorological phenomena. First, the different selected datasets of land surface temperature (LST), 2-m above ground air temperature (T2M), and precipitation are presented in Section 2. The methodology developed to define and compute the different climatological indicators is presented in Section 3. These indicators are then analysed and discussed in Section 4. Last, concluding remarks, limitations, and perspectives are given in Section 5.

Here we focus on the city of Paris, located in the administrative region Île-de-France, in the north-centre of France. The city is built on the Paris basin, a fairly flat area of plains and hills surrounding the river Seine (Figure 1). As the capital of France, Paris is its most populated city with around 2.2 million inhabitants in the municipality and up to 12 million in its urban area (INSEE, 2018). However, its land use has remained quite stable since the end of the 1990s.

Several studies of Paris' climatology were completed during the second part of the 20th century: Maurain (1947), Pédelaborde (1957) commented by Blanchet (1961), Grisollet (1958), Requillard (1961), De Félice and Schremmer (1964), Dettwiller (1970) commented by Loup (1971), Bessemoulin (1981), Dettwiller and Changnon Jr (1976), Calvet (1984), Escourrou (1984a, 1984b), Cantat (1985), Escourrou (1990, 1991), Choisnel and Vivier (1993), Thielen et al. (2000), Cantat (2004), and Coquillat et al. (2013). They describe the Paris basin as an area at the boundary between continental and strong oceanic influences with lower precipitation compared to the mean of the country (between 500 and 800 mm against 900 mm; Canellas *et al.*, 2014). Summers are relatively hot (18.8) and winters mild (4.4°C, average over the period 1981–2010 at the Paris-Montsouris station, Figure 1). Some studies focused on the urbanization and found different impacts such as a mean UHI of 3°C over the period 1971–1980 with maxima exceeding 10°C (Cantat, 2004) or increased precipitation downwind of the city (Escourrou, 1984a, 1984b).

2 | DATA

2.1 | Land surface temperature

As Tomlinson *et al.* (2011) pointed out in their review, the amount of remote sensed and especially satellite-derived data has seen a great increase in the past 20 years. The first studies analysing the effect of cities on LST go back to the 1970s (Rao, 1972; Matson *et al.*, 1978; Price, 1979); some of them were reviewed by Gallo *et al.* (1995). This temporal depth of LST products now enables the investigation of
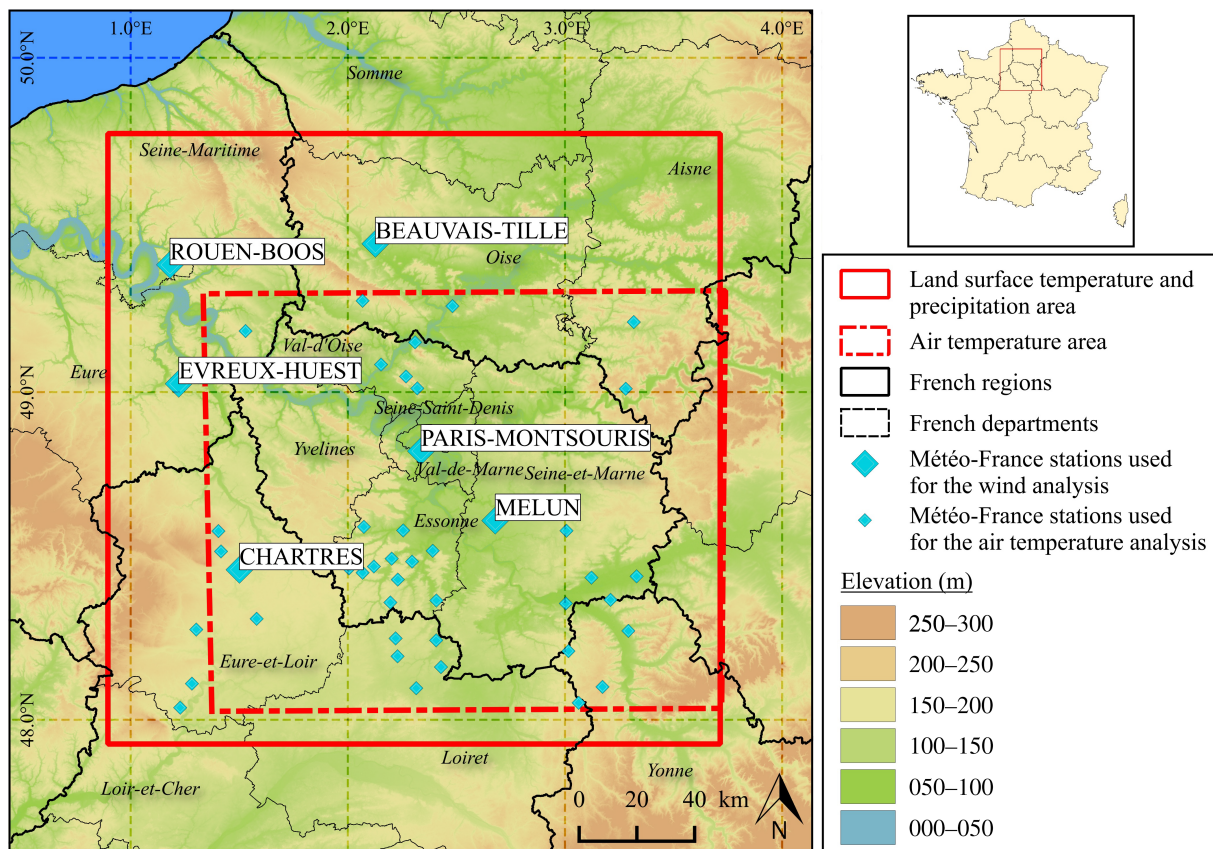
FIGURE 1 Map of the city of Paris and the areas studied for the land surface temperature (MODIS), air temperature, and precipitation (COMEPHORE) analysis

urban phenomena on a climatological time scale. Nonetheless, the majority of studies has been made on short time period (Zhou *et al.*, 2019) either because of the number of cloud-free images (Streutker, 2002, 2003; Weng, 2003; Jin *et al.*, 2005; Zhang and Wang, 2008; Schwarz *et al.*, 2012) or to analyse particular phenomena such as heat waves (Zaitchik *et al.*, 2006; Dousset *et al.*, 2011; Buscail *et al.*, 2012; Tomlinson *et al.*, 2012) or seasonal variation of the Surface Urban Heat Island (SUHI) (Chen *et al.*, 2006; Yuan and Bauer, 2007). Other studies took advantage of the potentially high number of images to analyse continuous evolution on multiple years (Jin, 2004; Zaitchik et al., 2014). Table 1 lists the main sensors carried by satellites currently used for SUHI studies in chronological order with a focus on free data and polar-orbiting satellites (MSG-SEVIRI is shown as an example of geostationary satellite).

While Landsat "is the longest running uninterrupted Earth observation program" (Wulder *et al.*, 2016) and the most used data for SUHI studies (Zhou *et al.*, 2019), the Moderate Resolution Imaging Spectroradiometer (MODIS) could represent in theory the biggest source of data by collecting two images per day on board the Terra and Aqua satellites since 2000 and 2002, respectively. The MODIS

products (Justice *et al.*, 1998) combine an acceptable spatial resolution of about 1 km (nadir) for urban climate studies, a temporal resolution of two images per satellite per day, and a time depth of 18 years. This makes it the best compromise between high spatial resolution sensors such as Landsat's Enhanced Thematic Mapper (ETM+) which reaches a 60-m resolution at nadir but provides only one image every 16 days, and high temporal resolution ones such as Meteosat's Spinning Enhanced Visible and Infrared Imager (SEVIRI) which provides images every 15 min with a lower spatial resolution of about 3 km at nadir.

In this study, the daily LST MODIS products MOD11A1 (Terra) and MYD11A1 (Aqua) are used between 2000 and 2016. They are derived from measurements of the brightness temperature at the top of the atmosphere using thermal infrared bands (10.78–11.28 μm and 11.77–12.27 μm) with a generalized split-window algorithm (Wan and Dozier, 1996). These products have been tested by multiple studies (Wan, 2002, 2008, 2014; Wan *et al.*, 2004; Coll *et al.*, 2005, 2009) indicating an accuracy better than 1°C in most cases. Version 005 of the MYD11A1 product has been evaluated over several areas worldwide including Paris, France (Wan, 2014). Results show a mean standard deviation of LST errors of about 0.4°C over urban areas and 0.6°C over cropland for

TABLE 1 List of potential sources of data on land surface temperature from polar orbiting satellites. P stands for "present" meaning that the satellite is still operational in 2019

Sensor	Satellite	Operator	Resolution (nadir)	TIR bands (µm)	Revisit	Equator crossing time (local solar time)	Period
AVHRR-1/2	TIROS-N	NOAA	1.1 km	(4) 10.3–11.3 (5) 11.5–12.5	11 days	15:30	1979–1981
AVHRR-3	NOAA-7 to 19	NOAA	1.1 km	(4) 10.3–11.3 (5) 11.5–12.5	11 days	–	1981-p
TM	Landsat 4 and 5	NASA NOAA	120 m	(6) 10.4–12.5	16 days	09:45	1982–2013
ETM+	Landsat 7	NASA USGS	60 m	(6) 10.4–12.5	16 days	10:00	1999-p
TIRS	Landsat 8	NASA USGS	100 m	(10) 10.6–11.19 (11) 11.5–12.51	16 days	10:00	2013-p
ASTER	Terra	NASA	90 m	(10) 8.125–8.475 (11) 8.475–8.825 (12) 8.925–9.275 (13) 10.25–10.95 (14) 10.95–11.65	1 day 1 night	On demand	2000-p
MODIS	**Terra**	NASA	1 km	(31) 10.78–11.28 (32) 11.77–12.27	1 day 1 night	10:30 22:30	2000-p
MODIS	**Aqua**	NASA	1 km	(31) 10.78–11.28 (32) 11.77–12.27	1 day 1 night	13:30 01:30	2002-p
AATSR	Envisat	ESA	1 km	11 12	35 days	10:00	2002-2012
AVHRR-3	MetOp-A,B and C	ESA EUMETSAT	1.1 km	(4) 10.3–11.3 (5) 11.5–12.5	29 days	09:30	2006-p
VIIRS	Suomi NPP	NASA DoD NOAA	750 m	(14) 8.4–8.7 (15) 10.263–11.263 (16) 1.538–12.488	16 days	10:30	2011-p
VIIRS	NOAA-20	NOAA	750 m	(14) 8.4–8.7 (15) 10.263–11.263 (16) 1.538–12.488	16 days	13:30	2017-p
SLSTR	SENTINEL 3 A and B	ESA	1 km	(7) 3.7 (8) 10.85 (9) 12	< 2 days	10:00	2016-p
SEVIRI	**MSG**	ESA EUMETSAT	3 km	10.8 12	Geos.	Every 15 min	2005-p

Note: MSG is shown as an example of geostationary satellite. Products used for this study are highlighted in bold.

23 cases. Here, version 006 (Wan *et al.*, 2015) of both products is used which is described as "much better than the previous C4.1 and C5 products" by Wan (2014). In addition to LST and emissivity, both products provide, for each pixel, a quality control assessment, a viewing time, and a viewing angle. For this study, the LST images are analysed by keeping the original projection system, that is, MODIS Sinuoïdal (SR-ORG:6842) with a spatial resolution of 926 m. Note that pixels with an estimated error greater than 2°C are removed.

TABLE 2 Mean I_{UHI} for different thresholds of missing urban (P_{murb}) and rural (Pmrur) pixels, for summer daytime

P_{mrur}	P_{murb} 0	10	20	30	40	50	60	70	80	90	100
0	3.5	3.5	3.5	3.5	3.5	3.5	3.5	3.5	3.5	3.5	3.5
10	3.9	4.1	4.2	4.2	4.2	4.2	4.2	4.2	4.2	4.2	4.2
20	4.0	4.3	4.3	4.3	4.3	4.3	4.3	4.3	4.2	4.2	4.2
30	4.0	4.4	4.4	4.4	4.4	4.4	4.3	4.3	4.2	4.2	4.2
40	4.0	4.4	4.4	4.5	4.4	4.4	4.3	4.3	4.1	4.1	4.0
50	4.0	4.4	4.4	4.4	4.3	4.3	4.2	4.1	4.0	3.9	3.8
60	4.0	4.4	4.4	4.4	4.3	4.3	4.2	4.1	3.9	3.7	3.6
70	4.0	4.4	4.4	4.4	4.3	4.3	4.2	4.1	3.8	3.6	3.3
80	4.0	4.4	4.4	4.4	4.3	4.3	4.1	4.0	3.7	3.4	3.0
90	4.0	4.4	4.4	4.4	4.3	4.2	4.1	4.0	3.7	3.4	2.8
100	4.0	4.4	4.4	4.4	4.3	4.2	4.1	4.0	3.7	3.4	3.4

Note: Colours represent combination of thresholds where more than 300 (light grey) and 500 (dark grey) images remain.

2.1.1 | MODIS' potential for LST climatology

The periods investigated in this study start on 2nd to 4th February, 2000 for Terra and July 4th, 2002 for Aqua and both end on December 31st, 2016. A total of 6,092 and 5,285 images from Terra and Aqua are available but many of them have some missing pixels. This is mainly due to the LST retrieval method which requires cloudless conditions, but also to the uncertainties associated with estimating the surface emissivity and the effects of viewing angles. A careful selection of those images must be done with the dual objective of being able to calculate good-quality SUHI indicators and to retain enough images to analyse the SUHI phenomenon on a climatological time scale. Nevertheless, it is important to emphasize that these LST products derived from clear-sky satellite measurements are representative of some specific atmospheric situations. This can induce a selection bias towards weather type prone to SUHIs and is a limitation of all remote sensed studies. Concerning viewing angles, a sensitivity study (not presented here) showed that they all could be retained because of their low impact on LST's climatologies.

The calculation of SUHI indicators imposes a selection based on the percentage of missing pixels in urban and rural areas simultaneously. Pixels can be missing either because of the presence of clouds, or because of their removal due to their estimated error. A sensitivity study on the choice of urban and rural thresholds was carried out, by comparing the number of remaining images and the corresponding mean SUHI (computed following the method presented in Section 3.2), separately for winter and summer, and for day and night. As an example, Table 2 presents the results for

TABLE 3 Number of MODIS images before selection (N_{tot}), after selection (N_{sel}), and the corresponding selection percentage (P_{sel}), for wintertime and summertime and separately for night and day

	Day			Night		
	N_{tot}	N_{sel}	P_{sel}	N_{tot}	N_{sel}	P_{sel}
DJF	2,754	327	12%	2,754	589	21%
JJA	2,872	593	20%	2,872	419	14%

summer daytime. The urban threshold appears to be relatively more constraining than the rural one with a greater impact on the number of images remaining. Low thresholds retain many images, but a number of them are significantly affected by clouds, which gives much lower SUHI intensities on average than with higher thresholds. In this case, the low number of pixels available for SUHI indicators calculation may lead to a misquantification of the phenomenon, depending on the location of these pixels in urban and rural areas. Conversely, too strict thresholds return too few images that furthermore correspond to very specific meteorological situations with stable atmosphere and no clouds for which the SUHI is the strongest. Between these two extremes, the SUHI intensity is quite steady with a slight trend towards higher intensity the stricter the urban threshold is. Between the 40 and 60% thresholds, the differences in SUHI intensities are on average less than 0.1°C with a maximum of 0.3°C for summer nights. An intermediate threshold of 50% was finally chosen, which makes it possible to retain enough workable images for the calculation of climatological SUHI indicators representative of each season (Table 3). Despite a ranging from 79 to 88%, between 1,947 and 2,583 images are kept over the entire time period covered, that is, on average 20–37 images per season per year.

Wintertime conditions are the most restrictive because they are generally more cloudy.

2.1.2 | MODIS' representativeness of the diurnal cycle

The Terra and Aqua satellites have a Sun-synchronous orbit and are assumed to cross the equator, respectively at 10:30, 22:30, and 13:30, 01:30. The passing time is provided for both products for each pixel as local solar time. A specific and unique time is associated with each image and converted to Coordinated Universal Time (UTC) by subtracting the longitude of the study area's centre divided by 15 (Williamson *et al.*, 2013). Overpass time is quite variable from 1 day to another but ranges between 2 hr on average with mean values of 02:02 and 12:37 for Aqua and 11:06 and 21:44 for Terra.

The representativeness of the diurnal cycle by MODIS products is evaluated by comparison with the LST product of SEVIRI carried on Meteosat Second Generation satellites (MSG). MSG is a geostationary satellite allowing SEVIRI to scan half of the earth continuously. This product, also based on a generalized split-window algorithm (Sobrino and Romaguera, 2004), has a spatial resolution of about 3 km at nadir and a temporal resolution of 15 min. It has been evaluated (Freitas *et al.*, 2009) and compared to others LST products by multiple studies (Trigo *et al.*, 2008; Gao *et al.*, 2012; Qian *et al.*, 2013; Duan and Li, 2015). To compare both datasets, the same selection made on MODIS LST is applied on SEVIRI LST, and only the common dates are retained. Duan and Li (2015) found that SEVIRI LST are on average warmer than MODIS LST over natural areas especially during the day (2–4°C against 1–2°C during the night). The findings obtained here over the Paris region for the 2006–2015 period are quite consistent: SEVIRI is on average warmer than MODIS by 0.52°C for Aqua and 1.98°C for Terra during the night, and by 1.76°C for Aqua and 1.56°C for Terra during the day (Figure 2). Differences in LST between the two products are probably related to both the higher spatial resolution of MODIS compared to SEVIRI and the different viewing angles. Nonetheless, SEVIRI data make it possible to retrieve the daily cycle of LST and to determine the hour of minimum and maximum daily LST. It is shown that MODIS overpass times capture these minimum and maximum daily LST well. Aqua night is a bit early before the minimum but the difference is relatively small and Terra and Aqua day encompass the end of the morning rise and the daily peak LST. In conclusion, MODIS LST products are well adapted both in terms of temporal and spatial resolution in order to study nighttime and daytime SUHIs, while providing time series consistent enough for climatological analyses.
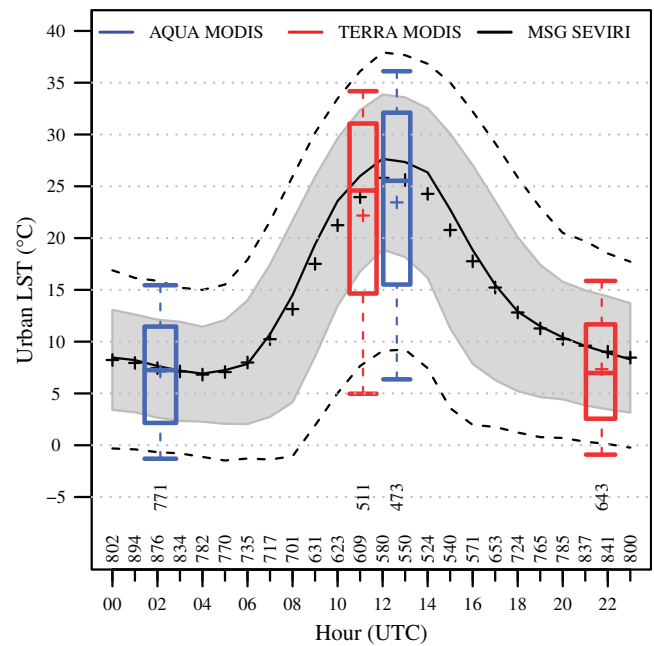

FIGURE 2 Comparison of urban LST distributions over 2006–2015 derived from MODIS (Aqua and Terra) and from SEVIRI data. SEVIRI data are plotted as diurnal cycle. The thick line is the mean, with the shaded area delimiting the 25th–75th percentiles data range, and lower and upper dashed lines the 10th and 90th percentiles. MODIS Aqua and Terra data are presented as boxplots, centred on the satellite mean passing time, with boxes extending from 25th to 75th percentiles and whiskers indicating 10th and 90th percentiles. Numbers above the *x*-axis represent the amount of images used for each hour. Both MODIS and SEVIRI data were selected following the method presented in Section 2.1.1. All SEVIRI hours were used for each day with a MODIS image available

2.2 | Air temperature

Several products of spatially interpolated near-surface air temperatures exist over the world at a relative coarse resolution but few over France on a kilometre scale (Canellas *et al.*, 2014). Moreover, to our knowledge, none of them take into account the urban environment and its impact on temperature. In this study, a new product developed at Météo-France by Kounkou-Arnaud and Brion (2018) is used. It takes into account both the elevation and the urban cover fraction coming from the ECOCLIMAP land cover database (Faroux *et al.*, 2013) to spatially interpolate daily minimum and maximum temperatures measured by 49 Météo-France stations (Givone, 1997). These stations are grouped into three categories depending on their corresponding urban cover fraction (f_{urb}): 40 rural stations ($f_{urb} < 0.3$), seven suburban stations ($0.3 \leq f_{urb} < 0.6$), and two urban stations ($f_{urb} \geq 0.6$). On a daily basis, a regression equation, with predictor selection, is computed linking minimum

temperature to elevation and urban cover fraction, if possible. Point errors from this equation are then used for residual kriging. The dataset is available for an 18 years period (2000–2017) at a spatial resolution of 1.25 km over the administrative region Île-de-France, thus, the studied area differs from the MODIS one (Figure 1).

2.3 | Precipitation

The product COMEPHORE (Tabary *et al.*, 2012) is used to investigate the possible effects of the city on precipitation. COMEPHORE is a 16-year database (1997–2012) of Quantitative Precipitation Estimations (QPE) over France with a temporal resolution of 1 hr and a spatial resolution of 1 km. The reanalysis is based on the 24 radars of the French network, giving pseudo-CAPPI (Constant Altitude Plan Position) images every 5 min with a resolution of 1 km over a 512×512 km area, and the hourly and daily rain rate from the rain gauge network. This reanalysis and the underlying data are detailed in Tabary (2007) and Tabary *et al.* (2012). For the present study, maps of daily precipitation are produced on a 200×200 km grid centred on Paris from the sum of the 24 hr QPE (Figure 1).

2.4 | Ancillary data

2.4.1 | Land cover

A knowledge of the land use and land cover is needed for the analysis of meteorological data, and especially for the separation of Urban and Rural masks. It is made here using the land cover classification from the global ECOCLIMAP-II database (Faroux *et al.*, 2013) based on both Corine Land Cover (CLC2000, EEA, 2005) and Global Land Cover (GLC2000, Bartholome and Belward, 2005). The combination of CLC2000 and GLC2000 maps the globe in 14 elementary classes that are in turn split into 273 more detailed classes. The product is provided with a resolution of $1/120°$ (≈ 1 km) and associated geographical coordinates. It is here resampled to the grid of each dataset by the nearest neighbour method. The mainland covers found over the study area are composed of different crops classes (79%), forest classes (11%), urban and built up areas (5%), and shrub covers (5%). The three main urban classes are suburban, dense urban, and industries and commercial areas. The methodology used to define the Urban and Rural masks differs depending on the application. It is presented in Section 3.1.1 for temperature and in Section 3.1.2 for precipitation.
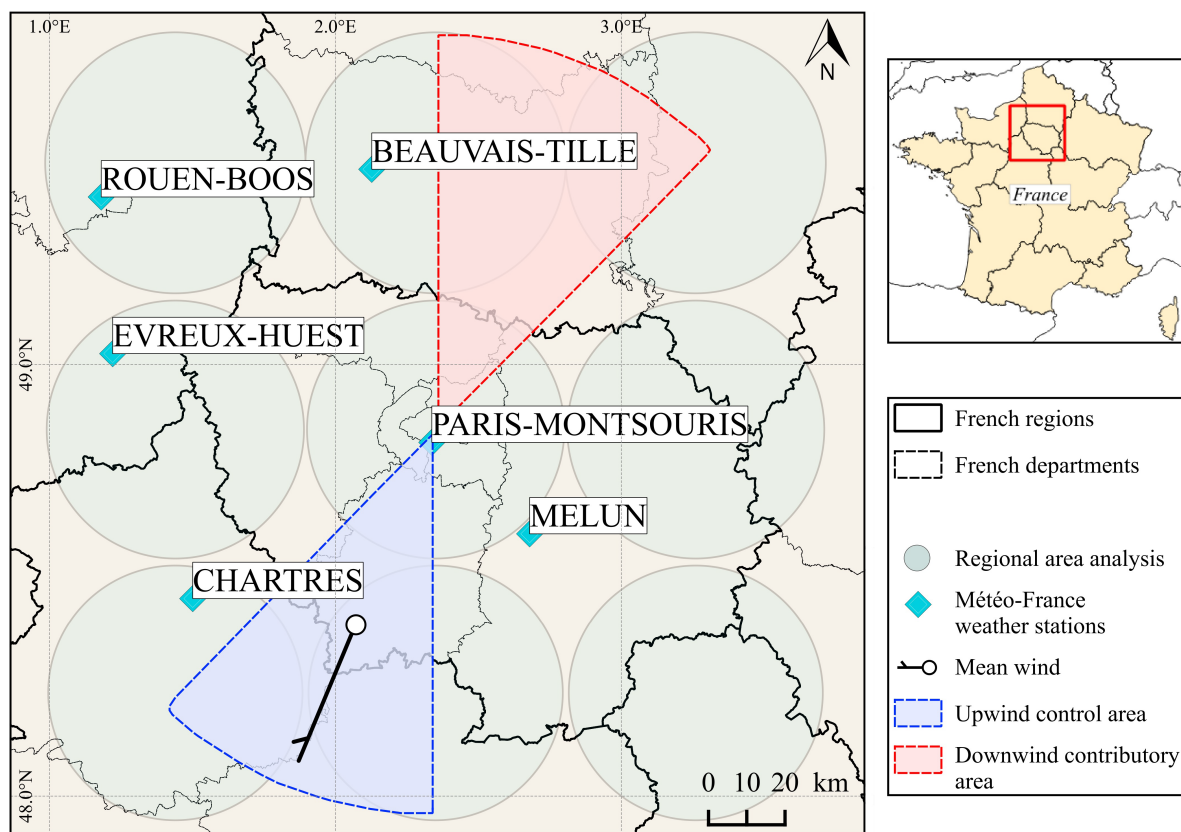

FIGURE 3 Map of the two circular sectors defined for precipitation analysis as upwind (control) area and downwind (contributory) area and oriented along the mean wind direction. The diamonds indicate the location of weather stations providing the long time series of wind measurements

2.4.2 | Wind data from weather stations

The day-by-day mean direction of the synoptic flow over the study area is needed to analyse the city effect on precipitation (detailed in Section 4.2). Five stations (Beauvais, Chartres, Evreux, Melun, and Rouen) of the Météo-France operational network are used to cover the study domain (see Figures 1 and 3). The wind components are computed independently by station from hourly data of wind direction and wind speed, and then averaged on a daily time frame and on the five stations.

3 | METHODOLOGY

3.1 | Definition of urban and rural masks

As presented in Section 2.4.1, the ECOCLIMAP-II land cover classification includes three main urban covers over the study domain that are merged into a single urban class. The remaining classes including various types of natural covers are gathered into a single class called rural class for simplicity.

3.1.1 | Application to temperature analysis

The UHI is an effect strongly governed by local land surface properties. Consequently, it can be calculated using urban and rural masks (defined according to land covers) that delimit the area potentially contributing to urban effects and the reference non-urban area, respectively. The study area covers a domain of 200×200 km which includes different urbanized areas such as the city of Rouen (see Figure 1). In order to focus on the UHI effect of the Paris urban area with respect to the surrounding rural zones, a smaller window containing Paris only is defined. This new area of 50×50 km covers both inner Paris and the near suburbs. Urban pixels inside this window build the Urban mask, while rural pixels outside build the Rural mask. Urban pixels outside the window, as well as rural pixels inside, are not considered.

3.1.2 | Application to precipitation analysis

For the analysis of urban effects on precipitation, the delimitation of contributory and reference geographic areas is more trickier than for temperature. The synoptic flow conditions and advection effects play a key role.

Previous studies have shown that the urban effect on precipitation is typically found downwind of cities (Shepherd, 2005). As a consequence, here we compare the mean precipitation in downwind and upwind areas of the city. These areas are defined as circular sectors with a radius of 100 km and an aperture angle of 45° that are oriented according to the daily mean wind direction presented in Section 2.4.2 (Figure 3).

The choice of the dimensions of the areas is based on three constraints. First as shown by Huff and Vogel (1978) and Shepherd (2005), the urban effect can be observed up to 75 km after the city, so the area downwind must be long enough. Second, the width of the area, that is, the chord length of the sector, should be about as large as the size of the city to capture all events that cross the city through either its centre or through the outskirts. Lastly, downwind and upwind areas must have equal surface area to have the same weight in the precipitation analysis based on spatial means.

3.2 | Urban heat island indicators

Schwarz et al. (2011, 2012) and Ward et al. (2016) reviewed different indicators for both SUHIs and UHIs. Some of them have the benefit of not relying on any assumption concerning the urban and rural areas, for example, the *magnitude* (maximum - mean) (Rajasekar and Weng, 2009; Schwarz et al., 2011, 2012) or the *range* (maximum–minimum) (Schwarz et al., 2012), but they are too sensitive to the inherent variability of the temperature and do not provide much relevant information when used on large areas. However, they could be interesting to investigate the heterogeneity of the temperature in the urban area. Other indicators such as the *gradient* (linear regression between temperature and distance from city centre) (Schwarz et al., 2012) or the ones derived from Gaussian fits (*area*, *magnitude*, *centre*) (Streutker, 2002, 2003; Tran et al., 2006; Schwarz et al., 2012, Quan et al., 2014) make significant assumptions regarding the shape of the city with urban area spreading evenly in every directions from the centre. Note that the Gaussian fit has been tested here, and returns an extent and a centre shifted away from Paris centre towards southeastern urbanized areas located on the banks of the river Seine.

For the present study, two indicators are selected, one representing the intensity and the other the spatial extent of the (S)UHI. Given that the air temperature data used in this study are spatially continuous, the indicators can be calculated the same way for UHI and SUHI. The intensity (I_{UHI}) is defined as the difference between temperature averaged on all pixels of the Urban mask and temperature averaged on all pixels of the Rural mask:

$$I_{\text{UHI}} = \bar{T}_{\text{urb}} - \bar{T}_{\text{rur}} \tag{1}$$

Note that the general notation I_{UHI} corresponds to the intensity of the UHI in air temperature when the indicator is computed using T2M or the intensity of the SUHI when the indicator is computed using LST. Thus, the temperature notation (T) used in Equations 1–3 refers to as T2M or LST.

The spatial extent of the (S)UHI is calculated two ways. The first indicator (SDE$_{\text{UHI}}$ for Standard Deviation Extent) is derived from the *hot island area* proposed by Zhang and Wang (2008) which looks at the number of pixels with a temperature greater than a threshold defined as the mean temperature of the studied area (T) plus a multiple of its standard deviation (σ_T) on a given day. This indicator does not depend on land covers nor city shape, but only on the statistical distribution of temperatures. For the present study, T and σ_T are computed from temperatures of all the pixels together in Urban and Rural masks (Section 3.1). SDE$_{\text{UHI}}$ is calculated as the proportion (in %) of urban pixels (P_{urb}) for which the temperature exceeds the given threshold in relation to the total number of urban pixels, with k an integer value (positive or negative) which defines the multiple of standard deviation:

$$\text{SDE}_{\text{UHI}}(k) = \frac{\sum P_{\text{urb}}[T \geq \bar{T} + k \cdot \sigma_T]}{\sum P_{\text{urb}}} \times 100 \tag{2}$$

The second indicator (TE$_{\text{UHI}}$ for temperature extent) follows the same principle but by applying a threshold in temperature degree (ΔT) and not on the basis of standard deviation:

$$TE_{\text{UHI}}(\Delta T) = \frac{\sum P_{\text{urb}}[T \geq \bar{T} + \Delta T]}{\sum P_{\text{urb}}} \times 100 \tag{3}$$

These two indicators are a way to define the area impacted by (S)UHIs. They range between 0 and 100%, with 100% meaning an image where the whole city experiences temperatures greater than the given threshold.

4 | RESULTS AND DISCUSSION

4.1 | Surface and air temperatures

The different UHI indicators are calculated for each day and each night of the complete time series of T2M maps (no data missing). Night and day SUHI indicators can be calculated only when MODIS images are available after selection. To compare SUHI and UHI, and to evaluate the possible effect of data selection on climatological analysis, the UHI indicators are studied using the complete dataset but also the subset corresponding to the selected dates.

Figure 4 shows the mean annual cycle of the three SUHI indicators along with the summer (JJA) and winter (DJF) means over the period 2000–2016. A greater annual variability is observed for I_{SUHI} during the day than at night (Figure 4b). Daytime I_{SUHI} varies between 0.92°C in September and 6.92°C in June that is, an amplitude of 6°C, whereas nighttime I_{SUHI} varies between 1.51°C in December and 3.43°C in July. The daytime I_{SUHI} seasonality can be explained by the combination of different processes. While the seasonal differences of daily urban LST are mainly governed by variations in the incoming solar radiation (Eliasson, 1996), it is the seasonal cycle of soil moisture that modulates the resulting cooling effect of vegetation on rural LST (Runnalls and Oke, 2000; Kalnay and Cai, 2003). This cooling effect is the lowest at the end of summer when soils are dry (Zhou et al., 2016). Consequently, the peak in I_{SUHI} observed in June, when the cooling effect is maximum due to vegetation evapotranspiration, is followed by a rapid decrease (−5.26°C) between June and August. On the other hand, because the cooling effect is less pronounced at night, the difference between urban and rural LST presents less seasonal variability, leading to more stable values of the I_{SUHI}. These results are consistent with the findings from Zhou et al. (2013) that showed the same seasonal pattern, but with lower I_{SUHI} values (4°C maximum in June). This gap may be due to different definitions of Urban and especially Rural masks. In their study, the Urban and Rural masks have the same surface area. Because the Rural mask they used is smaller than the one defined here, they may not take into account some areas with cooler LST, or they may over-represent warmer suburban areas. Note that for the present study, the effect of the size of the domain was investigated by comparing the indicators calculated on the entire area and on the reduced area covered by air temperature data (Figure 1). Since no significant difference was found, we are confident that we do not overestimate I_{SUHI}.

LST data show spatial variability over the study area that can fluctuate significantly by day and night ($\sigma_{\text{LST,DAY,ALL}}$ = 2.18°C and $\sigma_{\text{LST,NIGHT,ALL}}$ = 1.20°C), as well as by time of year ($\sigma_{\text{LST,DAY,JJA}}$ = 2.84°C, and $\sigma_{\text{LST,DAY,DJF}}$ = 1.16°C). Since the SDE indicator is built taking into account the temperature distribution, it is possible to compare SUHIs of different times of the day and seasons and to identify significantly hotter areas on a statistical basis.

SDE$_{\text{SUHI}}$ follows the same seasonal pattern as I_{SUHI} with a greater variability during the day than the night (Figure 4c). The fraction of the city impacted by a
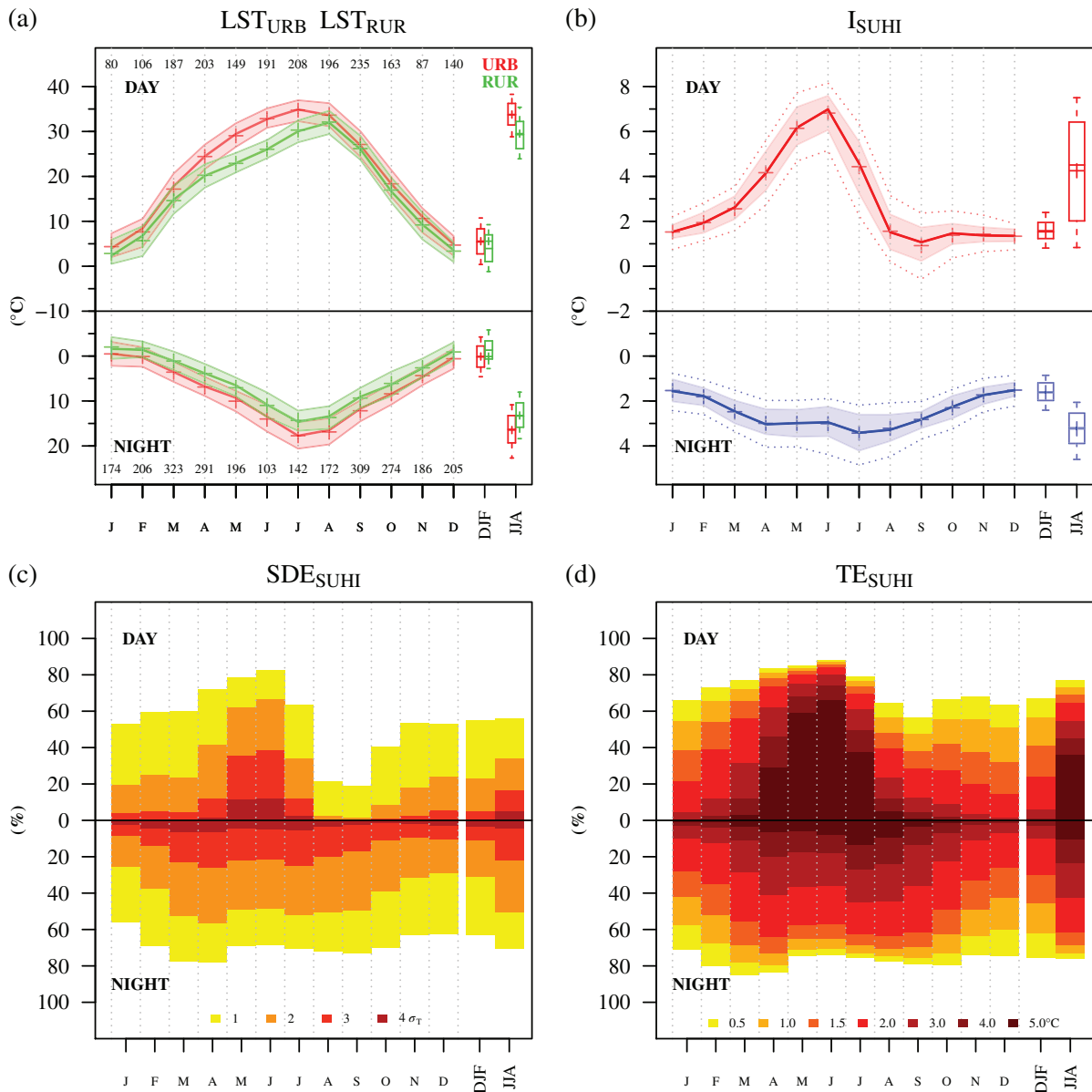
FIGURE 4 Monthly evolution of the urban and rural LST and the different SUHI indicators presented in Section 3.2 and calculated both for daytime (upper part) and nighttime (lower part). Numbers on the first chart represent the number of images used for each month

temperature excess of $1\sigma_T$ is maximum in June (82% of the total area) and minimum in September (19% only) at daytime. But on average over the year, the city is more consistently impacted at night than during the day for every σ_T thresholds except the last ($4\sigma_T$). Throughout the year, more than 60% of the city is impacted at night by what Zhou *et al.* (2013) refer to a *hot island* that is, an SDE$_{SUHI}$ greater than $1\sigma_T$. Nonetheless, the city's exposure to SUHIs decreases for higher thresholds. From the beginning of spring to the end of summer, the urban area that is impacted remains quite constant, for example, more than half of the city experiences an SDE$_{SUHI}$ of $2\sigma_T$, and a small part only an SDE$_{SUHI}$ of $4\sigma_T$ corresponding to the dense city core.

TE$_{SUHI}$ is based on fixed temperature thresholds ranging from 0.5 to 5°C (Figure 4d). Since the spatial amplitude (maximum–minimum) of LST is greater during the day than at night, a given threshold represents a greater proportion of the LST distribution at night. Consequently, it is more restrictive in identifying the impacted areas at night and does not represent the same phenomenon. For example, the maximum impacted area by the highest threshold (5°C) reaches 66% during the day in June but only 14% at night in July. The 66% represents a daily TE$_{SUHI}$ extending from the city centre to the inner suburbs, while the nighttime TE$_{SUHI}$ of 14% illustrates a more severe phenomenon concentrated in the dense urban centre. Contrary to the SDE indicator that suits the
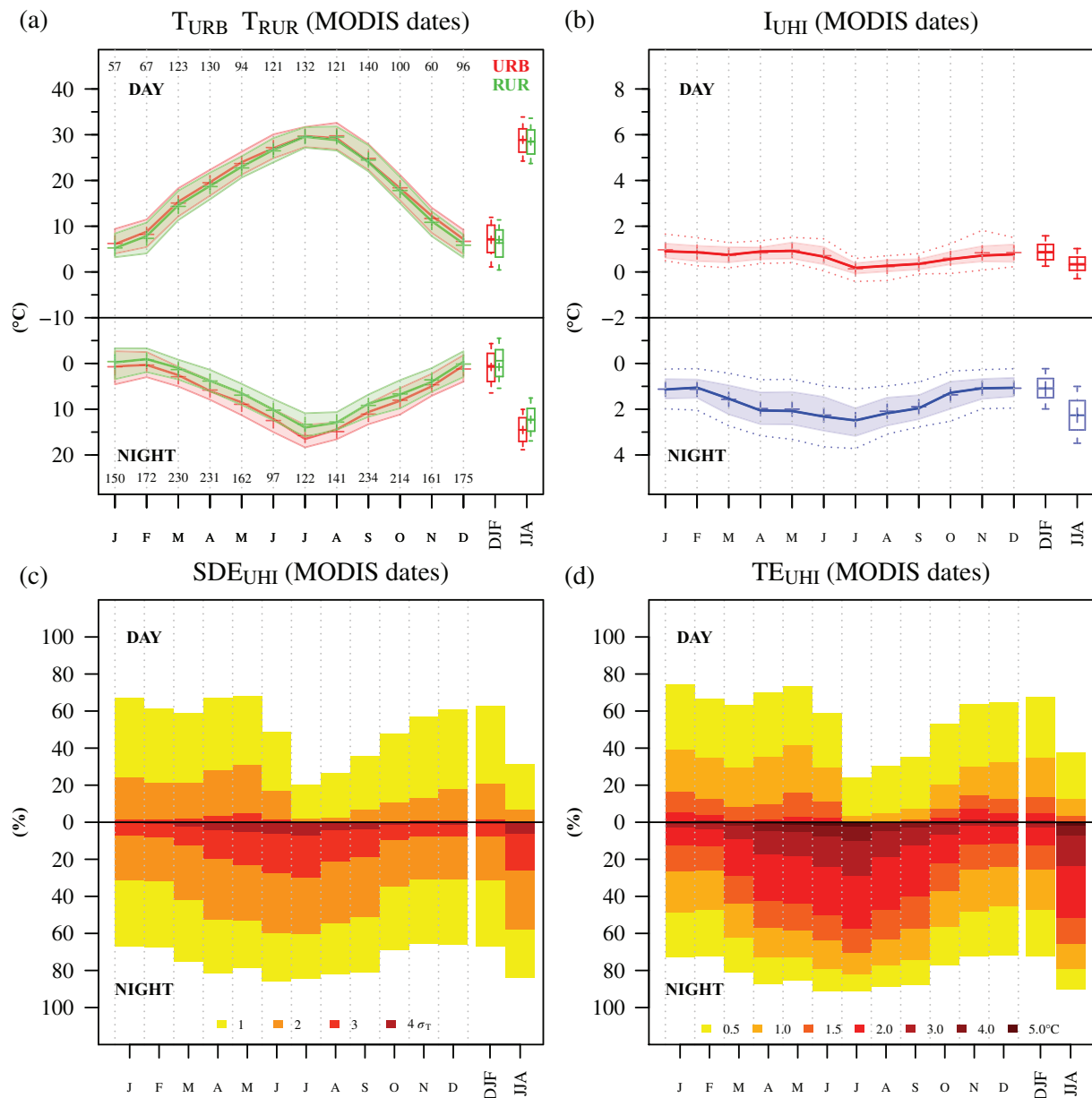
FIGURE 5 Monthly evolution of the urban and rural T2M and the different UHI indicators presented in Section 3.2 and calculated only on the dates selected for MODIS data analysis. Each chart presents the indicators calculated both for daytime (upper part) and nighttime (lower part)

comparison of day and night phenomena, since the TE indicator is computed on LST values rather than a statistical measure of the whole image it appears more illustrative, more easily understandable and thus better suited for impact studies and communication towards public stakeholders.

Figure 5 shows the same indicators computed from the T2M dataset on the same dates as the LST. It has been shown that LST and T2M are well correlated at higher scale (Prihodko and Goward, 1997). However, since LST are on average higher than T2M over natural (Mildrexler *et al.*, 2011) and urban areas (Nichol, 1996;

Voogt and Oke, 2003), I_{SUHI} is expected to be on average greater than I_{UHI} especially during the day. Unlike I_{SUHI}, I_{UHI} is systematically greater at night than during the day (Figure 5b). The maximum nighttime I_{UHI} is noted in July (2.45°C) whereas the daytime I_{UHI} is minimum (0.14°C). During the daytime, in cloudless conditions, the roughness of urban canopy and the heat accumulated in urban materials through incoming solar radiation generate dynamical- and thermal-induced turbulence. This leads to a more pronounced mixing in the urban boundary layer (UBL), which prevents urban T2M from getting warmer. Conversely, at night, by lack
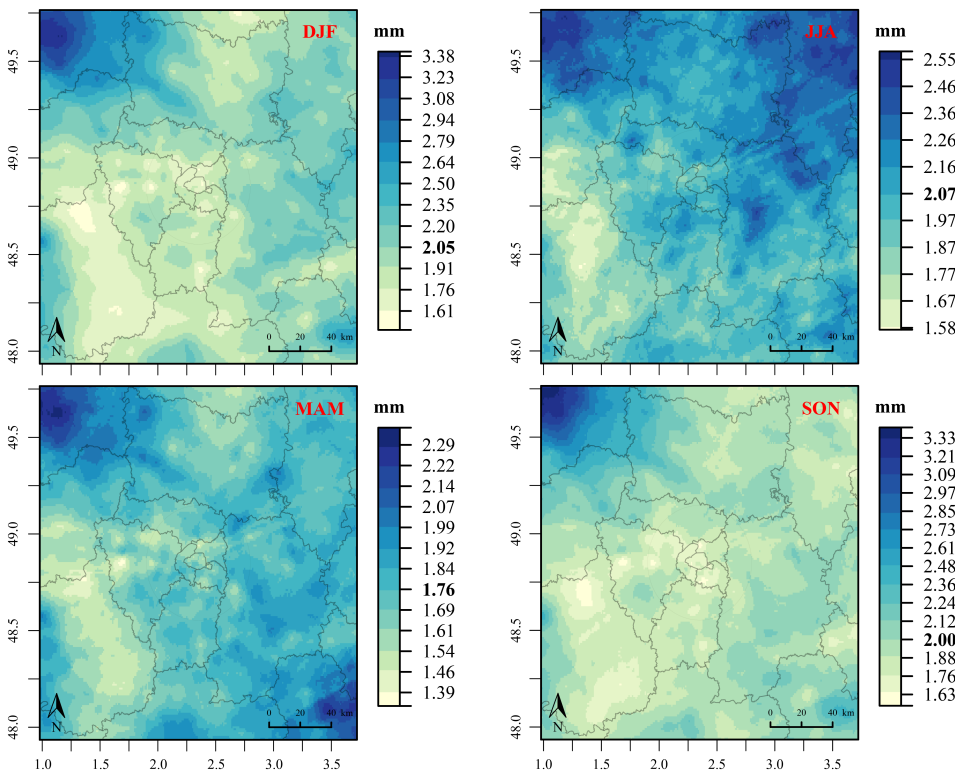
FIGURE 6 Seasonal maps of mean daily precipitation rate produced from the 1997–2012 COMEPHORE database. Values in bold represent the mean daily precipitation of the season and each classes correspond to 1/2 σ of its distribution. Thin lines represent French departments and the circle illustrates the urban extent

of both incoming solar radiation and turbulence, the UBL can become stable enough to induce an inversion layer resulting in higher T2M. The same seasonal variability is found for I_{UHI} as for I_{SUHI} during the night with a steady increase in spring and a maximum reached in the middle of summer. The intensities are comparable to that of the SUHI although slightly weaker. On the other hand, the seasonal dynamic of the daytime I_{UHI} is completely different from that of I_{SUHI}. It shows overall less variability throughout the year, with every season close to the annual mean except the end of summer and the beginning of autumn. It appears that the daily I_{UHI} is less driven by incoming solar radiation than the I_{SUHI} and more related to synoptic conditions. In the summer, the days are more subject to unstable atmosphere and turbulent fluxes resulting in more homogenized air temperatures and therefore lower UHI intensities. On the other hand, other seasons might be closer to neutral with more wind and a greater cloud cover. Moreover, the winter maximum could be explained by heat generated from anthropogenic fluxes. Dettwiller (1970) and Cantat (2004) already noted that in temperate oceanic climate, winter is the least favourable season for nighttime UHIs with stronger winds and less incoming solar radiation due to both solar elevation and cloud cover.

Both SDE_{UHI} and TE_{UHI} indicators calculated at nighttime evolve along the year according to two distinct modes: strong values are observed from March to

September and lower ones from November to February (Figures 5c,d). This translates to a more extended exposure of the city to UHIs in spring and summer than during the rest of the year: more than 40% of the city experiences UHIs of at least 2°C. Note that when computed on every date and not only on the dates selected for the MODIS data analysis, the different indicators show the overall same seasonal patterns with smoother evolution from one month to another and on average slightly lower values (not shown). This can be explained by the fact that the selected dates correspond to clear-sky nights and days that are potential cases of high (S)UHIs.

4.2 | Precipitation

To the best of our knowledge, there are no recent studies focusing on the precipitation of Paris. De Félice and Schremmer (1964) and later Moisselin *et al.* (2002) studied different long time series of precipitation from the Paris Observatory station and the Paris-Montsouris station, respectively, but did not find any significant trend, nor periodicity, due to the inter-annual variability. Douvinet *et al.* (2009) investigated the relationship between precipitation and flash floods on the Paris Basin but their area only intersects to the north of the domain studied here. Coquillat et al. (2013) examined the spatial distribution of lightning ground flashes around Paris and found higher activity over and downwind of the city in the
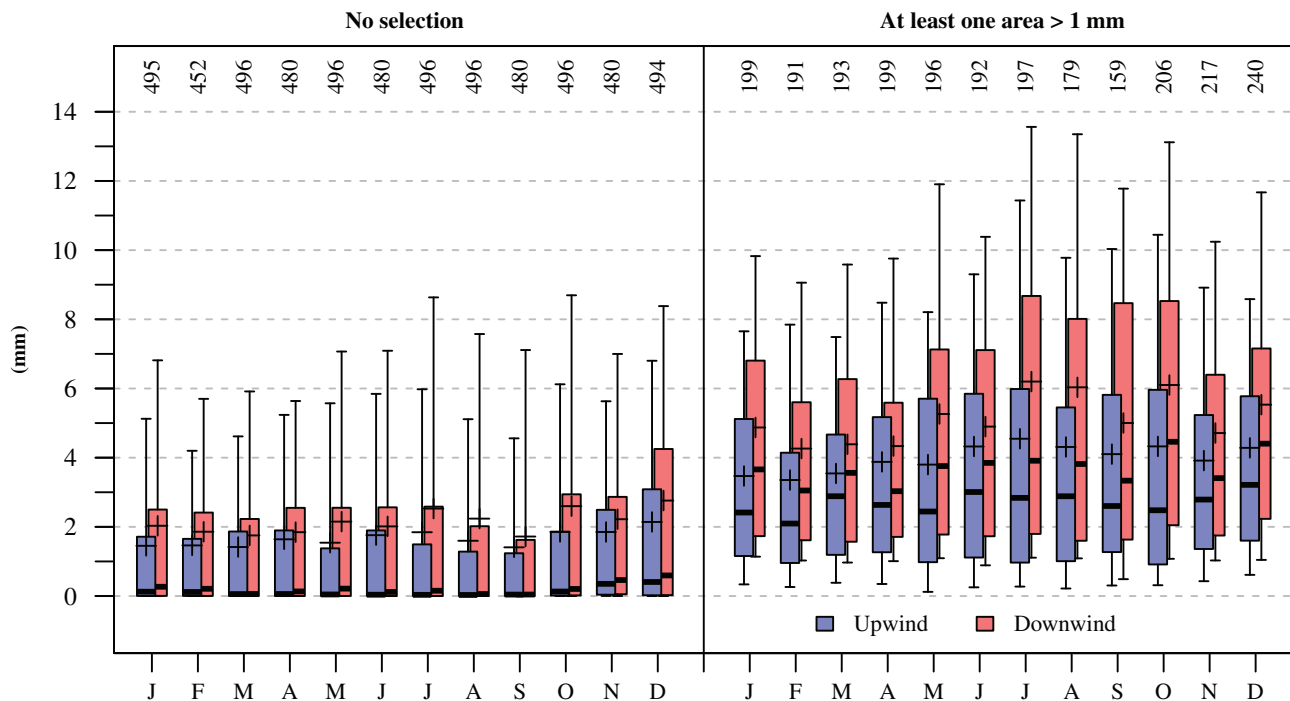
FIGURE 7 Comparison of the monthly evolution of the daily precipitation rates recorded during 1997–2012 time period over the upwind and downwind areas. The distributions of precipitation rates are presented as boxplots with boxes representing the 25th, 50th, and 75th percentiles, and whiskers the 10th and 90th percentiles. The crosses indicate the means. The comparison is carried out without selection of days (left panel) and for the rainy days only, that is, when at least one of the two analysis areas experiences precipitation rate ≥1 mm (right panel). The number of days involved each month is indicated at the top of the charts

prevailing wind direction that is, in the northwest. Canellas *et al.* (2014) analysed the climatology of precipitation over France with similar results as previous findings for Paris. While previous studies were based on a limited number of fixed stations, the COMEPHORE analysis (Section 2.3) enables a finer scale analysis of the precipitation spatial distribution, and for a long period covering 1997–2012. They first feed an analysis of the precipitation regional climatology, and then are used to investigate the potential urban effects on precipitation.

4.2.1 | Regional analysis

Seasonal maps of mean daily precipitation rate are produced from the 16-year COMEPHORE data (Figure 6). For the regional analysis, the study domain is divided into nine sectors (Figure 3) with the same surface area: northwest (NW), north (N), northeast (NE), west (W), center (C), east (E), southwest (SW), south (S), and southeast (SE). The sector with the highest daily precipitation rate is NW (2.34 mm against 1.96 mm on average over the whole area) which seems consistent with the Douvinet *et al.* (2009) findings. Conversely, the driest sectors are SW (1.77 mm) and W (1.76 mm). This pattern appears for every season, but is

accentuated in winter and autumn for NW and in spring for SW and W. Overall, the northern part has slightly more rain (2.11 mm on average for NW, N, NE) than the central and southern parts (1.89 mm for W, C, E and 1.88 mm for SW, S, SE). If we ignore the NW, because of its predominance in every season and for every wind direction, a stronger gradient appears from west to east with: 1.77 mm (W, SW), 1.9 mm (N, C, S), and 2.02 mm (NE, E, SE).

The spatial distribution of precipitation seems to be mainly driven by the synoptic wind direction and the regional atmospheric circulation that is, the rainiest days ($>$p75 $= 2.98$ mm) are associated with south-southwestern winds and the least rainy ones ($<$p25 $= 1.22 \times 10^{-3}$ mm) with north-northeastern winds. Other factors such as the hill effect described by Huff and Vogel (1978), the proximity to the coast (Daniels *et al.*, 2016), or the urbanization, could explain the maximum precipitation rate observed over NW sector which is both downwind of the city of Rouen and close to the sea.

4.2.2 | Urban influence

The influence of urbanization on precipitation is now a well-established phenomenon in the literature as described

by Shepherd (2005) in his review. Some of the authors cited earlier who described the climatology of Paris also noted the effect of the city on precipitation. Using the meteorological network of the area, Escourrou (1990) and Thielen et al. (2000) highlighted increased precipitation in the downwind part of the city in summer and reduced precipitation in the close upwind area.

To investigate the urban effects, the COMEPHORE data are here analysed by calculating for each day the daily precipitation rates in the upwind area (control area) and the downwind area (contributory area) of the city. The methodology developed to define these two areas depends on synoptic flow direction and is presented in Section 2.3. These daily precipitation rates are then averaged over the 1997–2012 time period for upwind and downwind areas to provide yearly and monthly trends. Without sorting on rainy or no rainy days, the daily precipitation is 2.15 mm downwind of the city against 1.67 mm upwind, that is, an increase of 29% (Figure 7). The same analysis is carried out by selecting rainy days, that is, for which at least one of both areas experiences daily precipitation ≥1 mm, that is 40% of the period (from 33% in September to 49% in December). In this case, the mean daily precipitation is 3.99 and 5.14 mm for upwind and downwind areas, respectively, that is, still an increase of 29%. This result is comparable to those of Shepherd *et al.* (2002) who found an increase of 28% in precipitation for major American cities. Figure 7 also shows that this effect appears for multiple types of precipitation events as illustrated by the different percentiles. For the more extreme events (p90 tail; Figure 7) on average 5.4 (9.2) mm are found upwind of the city and 7.13 (11.19) mm downwind without (with) selection, that is, an increase of 32 (22)%.

A monthly variability in precipitation is observed that is more important for downwind than upwind area. This means that the effect of the city on precipitation also varies with time, but always goes in the sense of an increase in precipitation in the downwind area. The urban effects are more marked between July and October with a maximum monthly increase in precipitation rate of 40% in August. Conversely, they are lower between March and June with a minimum monthly increase in precipitation rate of 12% in March. To explain this variability, we investigated the possible effects of both wind direction and wind speed but found no significant results. An apparent trend linking wind speed and rainfall amount might be solely explained by the fact that higher speeds are found with winds coming from the SW sector (where higher rainfall amounts are observed). In the same way, the highest urban effects observed with winds coming from the NE sector might be explained by overall low precipitation in both areas.

The evolution of precipitation and associated urban effects over the long time period covered by COMEPHORE

data is also investigated. It rains around 608 mm per year upwind of the city and 784 mm downwind. The three wettest years are 2001, 2000, and 1999 with respectively 849 (1043), 793 (972), and 770 (900) mm upwind (downwind) of the city. The three driest ones are 2011, 2005, and 2003 with 469 (637), 469 (646), and 482 (650) mm for the upwind (downwind) area. The same inter-annual variability is noted for both areas, but without any significant temporal trend over the 16 years.

5 | CONCLUSION

The climatologies of three urban phenomena that is, surface and air Urban Heat Island and enhancement of daily precipitation rates have been studied over the periods 2000–2016 and 1997–2012, respectively, on the city of Paris.

The potential of MODIS LST data has been investigated and deemed relevant for climatological analysis with between 20 and 37 images per season per year on average (Section 2.1.1). We found that SUHI intensities were greater during the day than at night, with annual maximum intensity occurring in June (6.92°C) where more than 60% of the city experiences an excess in LST greater than 5°C compared to the surrounding area (Section 4.1). Conversely, UHI intensities are highest at night with a maximum of 2.45°C reached in July. The SUHI and the UHI share the same nighttime seasonality but differ during the day due to different driving processes. SUHIs appear more driven by the differences in thermal properties between urban and rural environments as well as the city's complex geometry, whereas UHIs seem to be more influenced by general wind circulation and local turbulence.

A spatial gradient of precipitation rates over the Paris area from south–west to north–east has been observed, using the continuous COMEPHORE product of daily rain rates (Section 4.2.1). These spatial variations can be attributed to the global synoptic circulation and to the effect of the city which leads to an increase in precipitation downwind regardless of the season or the wind direction. On average this increase is 29% (Section 4.2.2).

Our results are quite consistent with those found in the literature in terms of intensity of the phenomena, seasonal variability, and the underlying physical processes. This confirms that spatialized data are well adapted for the study of urban climate at a kilometric scale. Nevertheless, some limitations remain that need to be taken into account for future studies. The use of satellite imagery for retrieving and analysing LST involves inherent issues regarding emissivity estimation, viewing angle, and anisotropy effects that need further research. As mentioned in Section 2.1.1, the selection of cloud free remote sensed

images induces a bias towards some specific atmospheric situations; and limits the climatological study of the SUHI for some weather types. On the other hand, the satellite-based LST products are particularly suitable for monitoring and studying heat waves.

Another issue, arising from the use of spatialized data for (S)UHI studies, is the definition of urban and rural environments. We showed that this definition could have a significant impact on the assessment of UHIs intensity. In this study, we chose Urban and rural masks fixed in time based on the fact that the city of Paris has seen a relatively small growth over the past decades. But this is not necessarily the case for all cities, nor if longer time periods are considered; so the urban expansion needs to be taken into account.

The databases that have been compiled and studied here constitute long series of gridded data particularly interesting for the evaluation of meso-scale meteorological models. In particular, they could be used to verify the capability of high-resolution regional climate models to simulate local climate and urban effects.

ORCID

Benjamin Le Roy 🔵 https://orcid.org/0000-0002-5496-2462

REFERENCES

Arnfield, A.J. (2003) Two decades of urban climate research: a review of turbulence, exchanges of energy and water, and the urban heat Island. *International Journal of Climatology*, 23(1), 1–26. https://doi.org/10.1002/joc.859.

Bartholome, E. and Belward, A.S. (2005) GLC2000: a new approach to global land cover mapping from earth observation data. *International Journal of Remote Sensing*, 26(9), 1959–1977. https://doi.org/10.1080/01431160412331291297.

Bessemoulin, J. (1981) Atlas climatique de la France, Édition réduite. In: *Direction de la Météorologie nationale, préparé et publié sous la direction de Jean Bessemoulin*. Paris: Ministère des transports, Secrétariat général à l'aviation civile, Direction de la météorologie. (In French).

Blanchet, G. (1961) Le climat du Bassin Parisien, d'après Pierre Pédelaborde. *Revue de Géographie Alpine*, 49(2), 373–378 (In French). https://www.persee.fr/doc/rga_0035-1121_1961_num_49_2_1992.

Buscail, C., Upegui, E. and Viel, J.F. (2012) Mapping heatwave health risk at the community level for public health action. *International Journal of Health Geographics*, 11(1), 38. https://doi.org/10.1186/1476-072X-11-38.

Calvet, C. (1984) *Climatologie de la région parisienne*. Paris: Ministère des transports, Direction de la météorologie. (In French).

Canellas, C., Gibelin, A.L., Lassègues, P., Kerdoncuff, M., Dandin, P. and Simon, P. (2014) Les normales climatiques spatialisées Aurelhy 1981-2010: températures et précipitations. *La météorologie*, 85, 47–55. (In French). https://doi.org/10.4267/2042/53750.

Cantat, O. (1985) Influence de l'urbanisation sur le climat de l'agglomération parisienne. *Physio-Géo-Géographie Physique et Environnement*, 16, 25–40. (In French). https://hal.archives-ouvertes.fr/hal-01155139.

Cantat, O. (2004) L'îlot de chaleur urbain parisien selon les types de temps. *Norois. Environnement, aménagement, société*, 191, 75–102. (In French). https://doi.org/10.4000/norois.1373,75,102.

Chen, X.L., Zhao, H.M., Li, P.X. and Yin, Z.Y. (2006) Remote sensing image-based analysis of the relationship between urban heat Island and land use/cover changes. *Remote Sensing of Environment*, 104(2), 133–146. https://doi.org/10.1016/j.rse.2005.11.016.

Choisnel, E. and Vivier, J.F. (1993) Les saisons météorologiques, le climat urbain les a-t-il masquées ? *Les Annales de la Recherche Urbaine*, 61, 47–50 Centre de Recherche d'Urbanisme. (In French). https://www.persee.fr/doc/aru_0180-930x_1993_num_61_1_1756.

Coll, C., Caselles, V., Galve, J.M., Valor, E., Niclos, R., Sánchez, J.M. and Rivas, R. (2005) Ground measurements for the validation of land surface temperatures derived from AATSR and MODIS data. *Remote Sensing of Environment*, 97(3), 288–300. https://doi.org/10.1016/j.rse.2005.05.007.

Coll, C., Wan, Z. and Galve, J.M. (2009) Temperature-based and radiance-based validations of the V5 MODIS land surface temperature product. *Journal of Geophysical Research: Atmospheres*, 114(D20), D20102. https://doi.org/10.1029/2009JD012038.

Coquillat, S., Boussaton, M.-P., Buguet, M., Lambert, D., Ribaud, J.-F. and Berthelot, A. (2013) Lightning ground flash patterns over Paris area between 1992 and 2003: Influence of pollution? *Atmospheric Research*, 122, 77–92.

Daniels, E.E., Lenderink, G., Hutjes, R.W.A. and Holtslag, A.A.M. (2016) Observed urban effects on precipitation along the Dutch west coast. *International Journal of Climatology*, 36(4), 2111–2119. https://doi.org/10.1002/joc.4458.

De Félice, P. and Schremmer, F. (1964) Étude de la variation des précipitations dans quelques stations de France et d'Algérie. *Archiv für Meteorologie, Geophysik und Bioklimatologie, Serie B*, 13(2), 173–192. (In French). https://doi.org/10.1007/BF02243251.

Dettwiller, J. (1970). *Évolution séculaire du climat de Paris: influence de l'urbanisation*. Paris: Direction de la Météorologie Nationale. (In French).

Dettwiller, J. and Changnon, S.A., Jr. (1976) Possible urban effects on maximum daily rainfall at Paris, St. Louis and Chicago. *Journal of Applied Meteorology*, 15(5), 517–519. https://doi.org/10.1175/1520-0450(1976)015<0518:PUEOMD>2.0.CO;2.

Dousset, B., Gourmelon, F., Laaidi, K., Zeghnoun, A., Giraudet, E., Bretin, P., Mauri, E. and Vandentorren, S. (2011) Satellite monitoring of summer heat waves in the Paris metropolitan area. *International Journal of Climatology*, 31(2), 313–323. https://doi.org/10.1002/joc.2222.

Douvinet, J., Planchon, O., Cantat, O., Delahaye, D. and Cador, J.M. (2009) Variabilité spatio-temporelle et dynamique des pluies de forte intensité à l'origine des «crues rapides» dans le Bassin Parisien (France). *Climatologie*, 6, 47–72. (In French). https://doi.org/10.4267/climatologie.511.

Duan, S.B. and Li, Z.L. (2015) Intercomparison of operational land surface temperature products derived from MSG-SEVIRI and Terra/aqua-MODIS data. *IEEE Journal of Selected Topics in Applied Earth Observations and Remote Sensing*, 8(8), 4163–4170. https://doi.org/10.1109/JSTARS.2015.2441096.

Eliasson, I. (1996) Urban nocturnal temperatures, street geometry and land use. *Atmospheric Environment*, 30(3), 379–392. https://doi.org/10.1016/1352-2310(95)00033-X.

Escourrou, G. (1984a) L'évolution du climat français: Océanisation et influence de l'urbanisation. *Revue Géographique de l'Est*, 24 (1), 17–26 (In French). https://www.persee.fr/doc/rgest_0035-3213_1984_num_24_1_1531.

Escourrou, G. (1984b) Quelques remarques sur la climatologie urbaine (Some remarks about urban climatology). *Bulletin de l'Association de Géographes Français*, 61(500), 83–97 (In French). https://www.persee.fr/doc/bagf_0004-5322_1984_num_61_500_5450.

Escourrou, G. (1990) La spécificité du climat de l'agglomération parisienne/The unique character of the Paris urban area's climate. *Géocarrefour*, 65(2), 85–89 (In French). https://www.persee.fr/doc/geoca_0035-113x_1990_num_65_2_5717.

Escourrou, G. (1991). *Le climat et la ville*. Paris: Nathan.

EEA. (2005) *Sustainable Use and Management of Natural Resources*. European Environment Agency: Technical report.

Faroux, S., Kaptué Tchuenté, A.T., Roujean, J.L., Masson, V., Martin, E. and Moigne, P.L. (2013) ECOCLIMAP-II/Europe: a twofold database of ecosystems and surface parameters at 1 km resolution based on satellite information for use in land surface, meteorological and climate models. *Geoscientific Model Development*, 6(2), 563–582. https://doi.org/10.5194/gmd-6-563-2013.

Freitas, S.C., Trigo, I.F., Bioucas-Dias, J.M. and Gottsche, F.M. (2009) Quantifying the uncertainty of land surface temperature retrievals from SEVIRI/Meteosat. *IEEE Transactions on Geoscience and Remote Sensing*, 48(1), 523–534. https://doi.org/10.1109/TGRS.2009.2027697.

Gallo, K.P., Tarpley, J.D., McNab, A.L. and Karl, T.R. (1995) Assessment of urban heat islands: a satellite perspective. *Atmospheric Research*, 37(1–3), 37–43. https://doi.org/10.1016/0169-8095(94)00066-M.

Gao, C., Jiang, X., Wu, H., Tang, B., Li, Z. and Li, Z. (2012) Comparison of land surface temperatures from MSG-2/SEVIRI and Terra/MODIS. *Journal of Applied Remote Sensing*, 6(1), 063606. https://doi.org/10.1117/1.JRS.6.063606.

Givone, C. (1997) Circulation et contrôle des données climatologiques à Météo-France. *La Météorologie*, 20, 31–40. (In French). https://doi.org/10.4267/2042/47031.

Grimmond, C.S.B. (2006) Progress in measuring and observing the urban atmosphere. *Theoretical and Applied Climatology*, 84 (1–3), 3–22. https://doi.org/10.1007/s00704-005-0140-5.

Grisollet, H. (1958) *Climatologie de Paris et de la région parisienne*. Paris: Direction de la météorologie nationale (In French).

Hu, L., Brunsell, N.A., Monaghan, A.J., Barlage, M. and Wilhelmi, O.V. (2014) How can we use MODIS land surface temperature to validate long-term urban model simulations? *Journal of Geophysical Research: Atmospheres*, 119(6), 3185–3201. https://doi.org/10.1002/2013JD021101.

Huff, F.A. and Vogel, J.L. (1978) Urban, topographic and diurnal effects on rainfall in the St. Louis region. *Journal of Applied Meteorology*, 17(5), 565–577. https://doi.org/10.1175/1520-0450(1978)017<0565:UTADEO>2.0.CO;2.

INSEE (2018). Recensement population 2016, Technical report, Institut national de la statistique et des études économiques. (In French) https://www.insee.fr/fr/statistiques/3681328?geo=COM-75056.

Jin, M. (2004) Analysis of land skin temperature using AVHRR observations. *Bulletin of the American Meteorological Society*, 85 (4), 587–600. https://doi.org/10.1175/BAMS-85-4-587.

Jin, M., Dickinson, R.E. and Zhang, D.A. (2005) The footprint of urban areas on global climate as characterized by MODIS. *Journal of Climate*, 18(10), 1551–1565. https://doi.org/10.1175/JCLI3334.1.

Justice, C.O., Vermote, E., Townshend, J.R., Defries, R., Roy, D.P., Hall, D.K., et al. (1998) The moderate resolution imaging Spectroradiometer (MODIS): land remote sensing for global change research. *IEEE Transactions on Geoscience and Remote Sensing*, 36(4), 1228–1249. https://doi.org/10.1109/36.701075.

Kalnay, E. and Cai, M. (2003) Impact of urbanization and land-use change on climate. *Nature*, 423(6939), 528–531. https://doi.org/10.1038/nature01675.

Kounkoud-Arnaud, R. and Brion, D. (2018) *Optimal interpolation of daily temperatures around Paris, taking into account urban fraction. 10th International Conference on Urban Climate*. New York, NY: American Meteorological Society. https://ams.confex.com/ams/ICUC10/meetingapp.cgi/Paper/341760.

Liu, Z., He, C., Zhou, Y. and Wu, J. (2014) How much of the world's land has been urbanized, really? A hierarchical framework for avoiding confusion. *Landscape Ecology*, 29(5), 763–771. https://doi.org/10.1007/s10980-014-0034-y.

Loup, J. (1971) Dettwiller (J.) - Évolution séculaire du climat de paris. influence de l'urbanisation. *Revue de Géographie Alpine*, 59(3), 382–383. (In French). https://www.persee.fr/doc/rga_0035-1121_1971_num_59_3_1240_t1_0382_0000_1.

Lowry, W.P. (1974) Project METROMEX: its history, status, and future. *Bulletin of the American Meteorological Society*, 55(2), 87–88.

Lowry, W.P. (1977) Empirical estimation of urban effects on climate: a problem analysis. *Journal of Applied Meteorology*, 16(2), 129–135. https://doi.org/10.1175/1520-0450(1977)016<0129:EEOUEO>2.0.CO;2.

Matson, M., Mcclain, E.P., McGinnis, D.F., Jr. and Pritchard, J.A. (1978) Satellite detection of urban heat islands. *Monthly Weather Review*, 106(12), 1725–1734. https://doi.org/10.1175/1520-0493(1978)106<1725:SDOUHI>2.0.CO;2.

Maurain, C. (1947) *Le climat de Paris*, Vol. 164. Paris: Presses universitaires de France (In French).

Mildrexler, D.J., Zhao, M. and Running, S.W. (2011) A global comparison between station air temperatures and MODIS land surface temperatures reveals the cooling role of forests. *Journal of Geophysical Research: Biogeosciences*, 116(G3), G03025. https://doi.org/doi:10.1029/2010JG001486.

Mills, G. (2014) Urban climatology: history, status and prospects. *Urban Climate*, 10, 479–489. https://doi.org/10.1016/j.uclim.2014.06.004.

Moisselin, J.M., Schneider, M. and Canellas, C. (2002) Les changements climatiques en France au XXè siècle. Etude des longues séries homogénéisées de données de température et de précipitations. *La météorologie*, 38, 45–56. (In French). https://doi.org/10.4267/2042/36233.

Nichol, J.E. (1996) High-resolution surface temperature patterns related to urban morphology in a tropical city: a satellite-based study. *Journal of Applied Meteorology*, 35(1), 135–146. https://doi.org/10.1175/1520-0450(1996)035<0135:HRSTPR>2.0.CO;2.

Oke, T.R. (1973) City size and the urban heat Island. *Atmospheric Environment*, 7(8), 769–779. https://doi.org/10.1016/0004-6981(73)90140-6.

Oke, T.R. (1982) The energetic basis of the urban heat Island. *Quarterly Journal of the Royal Meteorological Society*, 108(455), 1–24. https://doi.org/10.1002/qj.49710845502.

Oke, T.R. (1988) The urban energy balance. *Progress in Physical Geography*, 12(4), 471–508. https://doi.org/10.1177/030913338801200401.

Oke, T.R. (1995) The heat Island of the urban boundary layer: characteristics, causes and effects. In: *Wind Climate in Cities*. Dordrecht: Springer, pp. 81–107. https://doi.org/10.1007/978-94-017-3686-2_5.

Oke, T.R., Mills, G. and Voogt, J.A. (2017) *Urban climates*. Cambridge: Cambridge University Press.

Pédelaborde, P. (1957) *Le climat du Bassin Parisien: essai d'une méthode rationnelle de climatologie physique: Atlas*, Vol. 2. Paris, France: M.T. Génin. (In French).

Price, J.C. (1979) Assessment of the urban heat Island effect through the use of satellite data. *Monthly Weather Review*, 107(11), 1554–1557 https://doi.org/10.1175/1520-0493(1979)107<1554:AOTUHI>2.0.CO;2.

Prihodko, L. and Goward, S.N. (1997) Estimation of air temperature from remotely sensed surface observations. *Remote Sensing of Environment*, 60(3), 335–346. https://doi.org/10.1016/S0034-4257(96)00216-7.

Qian, Y.G., Li, Z.L. and Nerry, F. (2013) Evaluation of land surface temperature and emissivities retrieved from MSG/SEVIRI data with MODIS land surface temperature and emissivity products. *International Journal of Remote Sensing*, 34(9–10), 3140–3152. https://doi.org/10.1080/01431161.2012.716538.

Quan, J., Chen, Y., Zhan, W., Wang, J., Voogt, J. and Wang, M. (2014) Multi-temporal trajectory of the urban heat Island centroid in Beijing, China based on a Gaussian volume model. *Remote Sensing of Environment*, 149, 33–46. https://doi.org/10.1016/j.rse.2014.03.037.

Rajasekar, U. and Weng, Q. (2009) Urban heat Island monitoring and analysis using a non-parametric model: a case study of Indianapolis. *ISPRS Journal of Photogrammetry and Remote Sensing*, 64(1), 86–96. https://doi.org/10.1016/j.isprsjprs.2008.05.002.

Rao, P.K. (1972) Remote sensing of urban "heat islands" from an environmental satellite. *Bulletin of the American Meteorological Society*, 53(7), 647–648.

Requillard G. (1961). *De l'influence thermique de Paris et ses répercussions sur la banlieue proche*. Paris, France: Météorologie Nationale. (In French).

Roth, M., Oke, T.R. and Emery, W.J. (1989) Satellite-derived urban heat islands from three coastal cities and the utilization of such data in urban climatology. *International Journal of Remote Sensing*, 10(11), 1699–1720. https://doi.org/10.1080/01431168908904002.

Runnalls, K.E. and Oke, T.R. (2000) Dynamics and controls of the near-surface heat Island of Vancouver, British Columbia. *Physical Geography*, 21(4), 283–304. https://doi.org/10.1080/02723646.2000.10642711.

Schwarz, N., Lautenbach, S. and Seppelt, R. (2011) Exploring indicators for quantifying surface urban heat islands of European cities with MODIS land surface temperatures. *Remote Sensing of Environment*, 115(12), 3175–3186. https://doi.org/10.1016/j.rse.2011.07.003.

Schwarz, N., Schlink, U., Franck, U. and Großmann, K. (2012) Relationship of land surface and air temperatures and its

implications for quantifying urban heat Island indicators—an application for the city of Leipzig (Germany). *Ecological Indicators*, 18, 693–704. https://doi.org/10.1016/j.ecolind.2012.01.001.

Shepherd, J.M. (2005) A review of current investigations of urban-induced rainfall and recommendations for the future. *Earth Interactions*, 9(12), 1–27. https://doi.org/10.1175/EI156.1.

Shepherd, J.M., Pierce, H. and Negri, A.J. (2002) Rainfall modification by major urban areas: observations from spaceborne rain radar on the TRMM satellite. *Journal of Applied Meteorology*, 41(7), 689–701. https://doi.org/10.1175/1520-0450(2002)041<0689:RMBMUA>2.0.CO;2.

Sobrino, J.A. and Romaguera, M. (2004) Land surface temperature retrieval from MSG1-SEVIRI data. *Remote Sensing of Environment*, 92(2), 247–254. https://doi.org/10.1016/j.rse.2004.06.009.

Souch, C. and Grimmond, S. (2006) Applied climatology: urban climate. *Progress in Physical Geography*, 30(2), 270–279. https://doi.org/10.1191/0309133306pp484pr.

Streutker, D.R. (2002) A remote sensing study of the urban heat Island of Houston, Texas. *International Journal of Remote Sensing*, 23(13), 2595–2608. https://doi.org/10.1080/01431160110115023.

Streutker, D.R. (2003) Satellite-measured growth of the urban heat Island of Houston, Texas. *Remote Sensing of Environment*, 85(3), 282–289. https://doi.org/10.1016/S0034-4257(03)00007-5.

Tabary, P. (2007) The new French operational radar rainfall product. Part I: methodology. *Weather and Forecasting*, 22(3), 393–408. https://doi.org/10.1175/WAF1004.1.

Tabary, P., Dupuy, P., L'Henaff, G., Gueguen, C., Moulin, L., Laurantin, O., Merlier, C. and Soubeyroux, J.M. (2012) A 10-year (1997–2006) reanalysis of quantitative precipitation estimation over France: methodology and first results. *IAHS Publication*, 351, 255–260.

Thielen, J., Wobrock, W., Gadian, A., Mestayer, P. and Creutin, J.-D. (2000) The possible influence of urban surfaces on rainfall development: a sensitivity study in 2D in the meso-y-scale. *Atmospheric Research*, 54(1), 15–39. https://doi.org/10.1016/s0169-8095(00)00041-7.

Tomlinson, C.J., Chapman, L., Thornes, J.E. and Baker, C.J. (2012) Derivation of Birmingham's summer surface urban heat Island from MODIS satellite images. *International Journal of Climatology*, 32(2), 214–224. https://doi.org/0.1002/joc.2261.

Tomlinson, C.J., Chapman, L., Thornes, J.E. and Baker, C. (2011) Remote sensing land surface temperature for meteorology and climatology: a review. *Meteorological Applications*, 18(3), 296–306. https://doi.org/0.1002/met.287.

Tran, H., Uchihama, D., Ochi, S. and Yasuoka, Y. (2006) Assessment with satellite data of the urban heat Island effects in Asian mega cities. *International Journal of Applied Earth Observation and Geoinformation*, 8(1), 34–48. https://doi.org/10.1016/j.jag.2005.05.003.

Trigo, I.F., Monteiro, I.T., Olesen, F. and Kabsch, E. (2008) An assessment of remotely sensed land surface temperature. *Journal of Geophysical Research: Atmospheres*, 113(D17), D17108. https://doi.org/10.1029/2008JD010035.

UN United Nations. (2015) *World Urbanization Prospects: The 2014 Revision*. New York, NY: *United Nations Department of Economic and Social Affairs, Population Division*.

Voogt, J.A. and Oke, T.R. (2003) Thermal remote sensing of urban climates. *Remote Sensing of Environment*, 86(3), 370–384. https://doi.org/10.1016/S0034-4257(03)00079-8.

Wan, Z. (2002) Estimate of noise and systematic error in early thermal infrared data of the moderate resolution imaging Spectroradiometer (MODIS). *Remote Sensing of Environment*, 80(1), 47–54. https://doi.org/10.1016/S0034-4257(01)00266-8.

Wan, Z. (2008) New refinements and validation of the MODIS land-surface temperature/emissivity products. *Remote Sensing of Environment*, 112(1), 59–74. https://doi.org/10.1016/j.rse.2006.06.026.

Wan, Z. (2014) New refinements and validation of the collection-6 MODIS land-surface temperature/emissivity product. *Remote Sensing of Environment*, 140, 36–45. https://doi.org/10.1016/j.rse.2013.08.027.

Wan, Z. and Dozier, J. (1996) A generalized split-window algorithm for retrieving land-surface temperature from space. *IEEE Transactions on Geoscience and Remote Sensing*, 34(4), 892–905. https://doi.org/10.1109/36.508406.

Wan, Z., Hook, S. and Hulley, G. (2015) *MOD11A1 MODIS/Terra Land Surface Temperature/Emissivity Daily L3 Global 1km SIN Grid V006* [data set]. *NASA EOSDIS Land Processes DAAC*. https://doi.org/10.5067/MODIS/MOD11A1.006.

Wan, Z., Zhang, Y., Zhang, Q. and Li, Z.L. (2004) Quality assessment and validation of the MODIS global land surface temperature. *International Journal of Remote Sensing*, 25(1), 261–274. https://doi.org/10.1080/0143116031000116417.

Ward, K., Lauf, S., Kleinschmit, B. and Endlicher, W. (2016) Heat waves and urban heat islands in Europe: a review of relevant drivers. *Science of the Total Environment*, 569, 527–539. https://doi.org/10.1016/j.scitotenv.2016.06.119.

Weng, Q. (2003) Fractal analysis of satellite-detected urban heat Island effect. *Photogrammetric Engineering & Remote Sensing*, 69(5), 555–566. https://doi.org/10.14358/PERS.69.5.555.

Weng, Q. (2009) Thermal infrared remote sensing for urban climate and environmental studies: methods, applications, and trends. *ISPRS Journal of Photogrammetry and Remote Sensing*, 64(4), 335–344. https://doi.org/10.1016/j.isprsjprs.2009.03.007.

Williamson, S.N., Hik, D.S., Gamon, J.A., Kavanaugh, J.L. and Koh, S. (2013) Evaluating cloud contamination in clear-sky MODIS Terra daytime land surface temperatures using ground-based meteorology station observations. *Journal of Climate*, 26(5), 1551–1560. https://doi.org/10.1175/JCLI-D-12-00250.1.

Wulder, M.A., White, J.C., Loveland, T.R., Woodcock, C.E., Belward, A.S., Cohen, W.B., Fosnight, E.A., Shaw, J., Masek, J.G. and Roy, D.P. (2016) The global Landsat archive: status, consolidation, and direction. *Remote Sensing of Environment*, 185, 271–283. https://doi.org/10.1016/j.rse.2015.11.032.

Yuan, F. and Bauer, M.E. (2007) Comparison of impervious surface area and normalized difference vegetation index as indicators of surface urban heat Island effects in Landsat imagery. *Remote Sensing of Environment*, 106(3), 375–386. https://doi.org/10.1016/j.rse.2006.09.003.

Zaitchik, B.F., Macalady, A.K., Bonneau, L.R. and Smith, R.B. (2006) Europe's 2003 heat wave: a satellite view of impacts and land–atmosphere feedbacks. *International Journal of Climatology: A Journal of the Royal Meteorological Society*, 26(6), 743–769. https://doi.org/10.1002/joc.1280.

Zhang, J. and Wang, Y. (2008) Study of the relationships between the spatial extent of surface urban heat islands and urban characteristic factors based on Landsat ETM+ data. *Sensors*, 8(11), 7453–7468. https://doi.org/10.3390/s8117453.

Zhou, B., Lauwaet, D., Hooyberghs, H., De Ridder, K., Kropp, J.P. and Rybski, D. (2016) Assessing seasonality in the surface urban heat Island of London. *Journal of Applied Meteorology and Climatology*, 55(3), 493–505. https://doi.org/10.1175/JAMC-D-15-0041.1.

Zhou, B., Rybski, D. and Kropp, J.P. (2013) On the statistics of urban heat Island intensity. *Geophysical Research Letters*, 40(20), 5486–5491. https://doi.org/10.1002/2013GL057320.

Zhou, D., Xiao, J., Bonafoni, S., Berger, C., Deilami, K., Zhou, Y., et al. (2019) Satellite remote sensing of surface urban heat islands: progress, challenges, and perspectives. *Remote Sensing*, 11(1), 48. https://doi.org/10.3390/rs11010048.

Zhou, Y., Li, X., Asrar, G.R., Smith, S.J. and Imhoff, M. (2018) A global record of annual urban dynamics (1992–2013) from nighttime lights. *Remote Sensing of Environment*, 219, 206–220. https://doi.org/10.1016/j.rse.2018.10.015.

Zhou, Y., Smith, S.J., Zhao, K., Imhoff, M., Thomson, A., Bond-Lamberty, B., Asrar, G.R., Zhang, X., He, C. and Elvidge, C.D. (2015) A global map of urban extent from nightlights. *Environmental Research Letters*, 10(5), 054011. https://doi.org/10.1088%2F1748-9326%2F10%2F5%2F054011.